Atomic Spectroscopy

Article

Spectral Acquisition-Window Optimization for FL-LIBS Quantification of Cr, Mn, and Ni in Z3CN20-09M Steel

Qi Yang, [a] Jinna Mei, [d] Huaiqing Qin, [a] Yuhua Hang, [d] Zhimin Lu, [a] and Shunchun Yao [a,b,c,*]

[a] School of Electric Power Engineering, South China University of Technology, Guangzhou 510641, P. R. China

[b] Guangdong Province Key Laboratory of Heat and Mass Transfer and Low-Carbon Conversion, Ministry of Education, South China University of Technology, Guangzhou 510641, P. R. China

[c] Guangdong Engineering Technology Center for High-Efficiency and Low-Pollution Conversion of Energy, Guangzhou 510641, P. R. China

[d] Suzhou Nuclear Power Research Institute, Suzhou 215004, P. R. China

Received: *July 05, 2026;* ***Revised:*** *September 12, 2026;* ***Accepted:*** *September 12, 2026;* ***Available online:*** *September 26, 2026.*

DOI: 10.46770/AS.2026.0076s

ABSTRACT: High-repetition-rate fiber-laser-induced breakdown spectroscopy (FL-LIBS) supports rapid surface scanning, yet reliable alloy quantification depends on spectra that are stable and representative of the sampled surface. Here, a spectral acquisition-window optimization strategy was developed for quantifying Cr, Mn, and Ni in Z3CN20-09M steel. Each acquisition window was characterized by pulse accumulation number and acquisition-window length, and CRITIC-TOPSIS integrated multiple spectral-quality metrics to rank the scanning conditions. Three representative acquisition windows were compared using full-spectrum partial least squares regression (PLSR) models calibrated with 11 high-alloy steel certified reference materials. The 10 ms, 4 mm s^{-1} condition gave the best overall performance, with a 40 μm acquisition-window length that approximately matched the laser spot diameter and a moderate pulse accumulation number of 350. Under this condition, full-spectrum PLSR yielded RMSEPs of 1.170, 0.063, and 1.975 wt.% for Cr, Mn, and Ni, respectively, lower than those under the matched comparison conditions. Subsequent model optimization using mutual information-variable importance in projection PLSR (MI-VIP-PLSR) further reduced the RMSEPs to 0.552, 0.047, and 0.127 wt.%. MI-VIP retained compact subsets of chemically informative variables, improving model interpretability while preserving high prediction accuracy. These results link pulse accumulation and spatial sampling to quantitative accuracy and provide a physically interpretable strategy for rapid, reliable FL-LIBS alloy quantification.

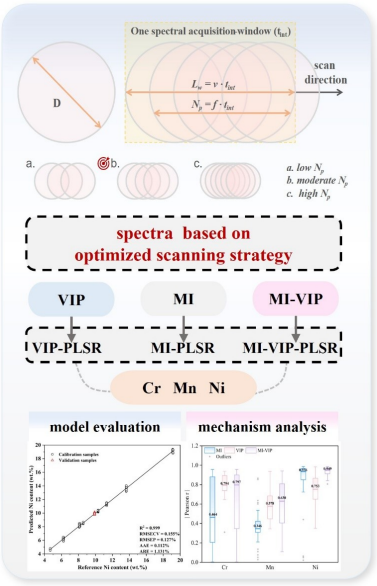

INTRODUCTION

The compositional integrity of reactor coolant piping is important for the safe operation of nuclear power plants. Z3CN20-09M cast duplex stainless steel is widely used for such piping, and its Cr, Mn, and Ni contents influence corrosion resistance and phase balance. Rapid verification of these alloying elements is therefore required during inspection and maintenance [1,2]. Conventional sampling followed by laboratory analysis can prolong planned outages and reduce unit availability [3-7]. A rapid in situ method is consequently needed to provide reliable elemental information within the available maintenance window.

Laser-induced breakdown spectroscopy (LIBS) has attracted considerable attention for field applications owing to its capability for rapid, simultaneous multi-element analysis [8,9]. Quantitative LIBS analyses of alloy element in steel have been extensively reported. Luna *et al.* compared partial least squares (PLS) models built from the full spectrum with PLS models using variables selected by variable importance in projection (VIP) and interval PLS for the determination of Cr, Ni, and Mn in steel samples. The relative standard errors of prediction were 3.81% for Cr, 6.22% for Ni, and 10.32% for Mn [10]. Wang *et al.* compared PLS with support

vector regression (SVR) for steel analysis. The SVR models yielded prediction set R^2 values of 0.993 for Mn and 0.995 for Cr, with root mean square errors (RMSE) of 0.044 and 0.045 wt.%, respectively [11]. Zhang *et al.* used SelectKBest to select spectral variables and subsequently developed backpropagation neural network (BPNN) models for the determination of Mn, Cr, and Ni. The resulting relative prediction errors were 1.13%, 2.85%, and 7.20%, respectively [12]. Portable configurations have also been explored. Zeng *et al.* developed a fiber-optic LIBS system incorporating a Q-switched Nd: YAG laser, which yielded calibration R^2 values of 0.9965 for Mn and 0.991 for Cr [13]. However, most of these studies relied on low-repetition-rate solid-state lasers and static or discrete sampling locations. Such designs do not directly address how spatially representative spectra can be obtained during rapid scanning. Maintaining reliable quantitative information while covering an inspected surface within a limited maintenance window therefore remains a practical bottleneck.

Fiber lasers offer compactness, high beam quality, and kHz repetition rates, making them attractive ablation sources for LIBS. Their use has enabled fiber-laser LIBS (FL-LIBS), which can acquire numerous spectra over a short period during rapid scanning and is therefore suitable for rapid field analysis of metallic surfaces [14,15]. Scharun *et al.* developed a hand-guided FL-LIBS instrument for the analysis of aluminum and iron alloys. With an acquisition time of 5 ms, the system could obtain measurements at nearly any position and achieved analytical performance comparable to that of a mobile spark discharge optical emission spectrometer [16]. Xu *et al.* examined the effects of spot overlap, non-overlapping ablated area, scanning speed, and pulse energy on the FL-LIBS analysis of aluminum alloys. After parameter optimization, the calibration models for Cu, Mg, and Mn achieved R^2 values above 0.998, with average relative errors below 5% [17]. Qu *et al.* further showed that integration time and scanning speed jointly affected spectral intensity and stability during continuous motion in a high-repetition-rate LIBS system. Parameter optimization yielded an aluminum-alloy classification accuracy of 97.71% [18]. Taken together, these studies demonstrate the potential of FL-LIBS for rapid measurements during scanning. However, previous studies have generally focused on individual acquisition parameters or isolated spectral responses evaluated under application-specific conditions, leaving the coupled effects of these factors insufficiently understood. In rapid scanning, integration time, scanning speed, and spot overlap jointly define the spectral acquisition-window, including the temporal interval and surface region contributing to each spectrum, and influence spectral intensity and stability [19]. Therefore, a systematic strategy is still needed to define and evaluate the spectral acquisition-window for rapid scanning, balancing spectral quality and stability against surface coverage.

The rapid acquisition of spectra by FL-LIBS creates a second challenge for quantitative analysis when calibration data are limited. High-frequency scanning can generate many spectra within a short time, but repeated spectra acquired from the same reference material do not add independent concentration levels to the calibration set. This imbalance between the high-dimensional spectral space and the limited independent concentration information increases data redundancy and can weaken the robustness and interpretability of quantitative models. Accordingly, with limited calibration samples, feature extraction is needed to reduce wavelength redundancy while retaining concentration-relevant information for alloy quantification [20,21]. Lu *et al.* applied a layered interval wrapper method to LIBS data from eight T91 steel specimens with different aging grades and seven 12Cr1MoV steel specimens with different grain-size grades. The method increased the classification accuracy for the T91 dataset from 0.76 to 0.92 for logistic regression and from 0.81 to 0.94 for support vector machines. For the 12Cr1MoV dataset, the corresponding accuracies increased from 0.69 to 0.87 and from 0.69 to 0.90, respectively [22]. Huang *et al.* used SelectKBest screening before multi-element quantification of 12 alloy steels. For nine alloying elements, the validation R^2 values ranged from 0.9920 to 0.9996, with prediction errors ranging from 0.0073 to 0.0270 wt.% [23]. Wang *et al.* used the least absolute shrinkage and selection operator (LASSO) to select wavelengths for quantifying Mn, Cu, Ni, Mo, and Ti in micro alloyed steels. The model based on the selected variables achieved a cross-validation R^2 of 0.996 and an RMSEP of 0.0053 wt.% for Cu [24]. Although recent studies have begun to include model interpretation, feature selection itself is still commonly driven by a single statistical criterion or by the predictive performance of a specific model. Such approaches prioritize either the association between individual wavelengths and analyte concentrations or their contribution to model prediction. The selected variables may improve numerical performance but are not always readily attributable to analyte emissions or chemically meaningful matrix responses. Therefore, a feature selection strategy that links concentration relevance, contribution to quantitative prediction, and the chemical origins of retained spectral regions needs to be further developed for alloy quantification.

To address these challenges, we developed a spectral acquisition-window optimization strategy for FL-LIBS quantification of Cr, Mn, and Ni in Z3CN20-09M steel. The spectral acquisition window was defined by pulse accumulation number and acquisition-window length, linking the integration time and scanning speed to temporal pulse accumulation and spatial surface coverage. CRITIC-TOPSIS was first used to rank scanning conditions according to spectral signal quality and stability. Then, three representative acquisition windows were evaluated using full-spectrum PLSR models calibrated with 11 certified high-alloy steel reference materials to determine whether the spectral-quality ranking translated into improved quantitative performance. Under the selected acquisition window, PLSR models based on the full spectrum and variables selected by VIP,

Table 1. Reference concentrations of the major elements in the high-alloy steel reference materials and the Z3CN20-09M specimen (wt.%)

No.	Sample ID	Reference concentrations							
		Cr	C	Si	Mn	P	Ni	Mo	Cu
1	KYBS364-25	17.01	0.134	1.06	1.51	0.033	8.56	0.062	0.16
2	KYBS317-25	16.4	0.061	0.38	1.15	0.033	10.32	2.04	0.164
3	KYBS325-25	25.56	0.018	0.452	0.756	0.021	6.24	3.48	0.091
4	KYBS378-16	18.08	0.068	0.613	1.27	0.032	8.170	0.114	0.09
5	KYBS378B-16	18.09	0.075	0.446	1.30	0.035	8.100	0.04	0.082
6	KYBS380-25	18.25	0.074	0.487	0.921	0.037	11.32	3.33	0.196
7	KYBS381-25	18.42	0.029	0.369	1.01	0.031	13.64	4.00	0.062
8	KYBS382-25	21.80	0.029	0.391	1.07	0.024	4.670	2.78	0.080
9	KYBS388-25	24.33	0.106	0.443	1.71	0.027	19.12	0.147	0.100
10	KYBS389-25	24.30	0.064	2.05	1.09	0.026	19.15	0.036	0.064
11	KYBS393-25	16.18	0.138	0.472	0.972	0.028	6.190	0.092	0.189
12	Z3CN20-09M	20.10	0.051	1.174	1.140	0.011	9.907	0.129	0.064

mutual information (MI), and MI-VIP were further assessed to optimize quantitation. This framework was designed to establish a physically interpretable link between FL-LIBS acquisition conditions and rapid, reliable alloy quantification.

EXPERIMENTAL

Samples. Eleven high-alloy steel certified reference samples obtained from NCS Testing Technology Co., Ltd. (China) were employed for calibration model development. Table 1 lists the reference concentrations of the major elements in the standard materials and the Z3CN20-09M specimen. The standard materials were selected to cover the concentration ranges of the target elements. The reference concentrations of Cr, Mn, and Ni in the Z3CN20-09M specimen were determined by spark optical emission spectrometry (Spark-OES). The Z3CN20-09M sample was subsequently analyzed as the target sample to assess the applicability of the developed quantitative models.

FL-LIBS system. The FL-LIBS spectra were acquired using the same experimental configuration as that described in our previous work.[25] A detailed description of the FL-LIBS system has been reported in the literature. Briefly, a Q-switched fiber laser operating at 1064 nm with a pulse duration of 120 ns was employed as the ablation source. In this study, the laser repetition rate was 35 kHz, and the laser was operated at 60% of its maximum nominal power of 20 W. The laser beam was focused onto the sample surface using a plano-convex lens to generate plasma. The plasma emission was collected laterally and introduced into a time-integrated spectrometer (AvaSpec-ultras2048-4, Avantes, Netherlands), which covered a wavelength range of 225-836 nm with a spectral resolution of 0.1-0.22 nm. Owing to the high repetition rate of the fiber laser, the plasma excitation interval was shorter than the minimum integration time of the spectrometer. Therefore, the spectrometer was operated in an internally triggered continuous acquisition mode. The integration time of the spectrometer and the translation speed of the motorized X-Y stage were optimized and are discussed in the later section. During spectral acquisition, the samples were placed on the motorized X-Y stage and translated along linear ablation paths to ensure continuous sampling from fresh surface regions. Before measurement, each sample surface was ground and polished using 400-grit sandpaper, followed by cleaning with alcohol. This pretreatment was performed to remove surface oxides and contaminants, thereby improving the representativeness and stability of the acquired spectra. Each scanning condition was evaluated using spatially separated linear ablation tracks, with 100 consecutive spectra acquired from each track. The sample stage was moved to a fresh surface region between tracks to avoid the influence of previous ablation.

Methods. ***Workflow.*** The workflow of this study is shown in Fig. 1. First, the spectral acquisition-window of the FL-LIBS system was characterized under different scanning conditions using pulse accumulation number and acquisition-window length. Multiple spectral-quality indicators were evaluated, and CRITIC-TOPSIS was applied to identify the candidate optimal scanning condition. The spectral averaging strategy was then determined by comparing spectral fluctuations at different averaging group sizes. To directly validate the acquisition-window optimization, spectra from the standard alloys and the Z3CN20-09M sample were collected under three representative scanning conditions. Full-spectrum PLSR models were constructed to compare their quantitative performance. Finally, spectra acquired under the selected acquisition window were used for quantitative model optimization. Full-spectrum, VIP-, MI-, and MI-VIP-selected PLSR models were evaluated to further improve the prediction accuracy for Cr, Mn, and Ni.

Spectral acquisition-window descriptors. Because the FL-LIBS system operated at a high laser repetition rate and the spectrometer worked in continuous integration mode, each spectrum was formed by the accumulated emission from multiple laser pulses over a finite scanned surface length. In this work, this process was

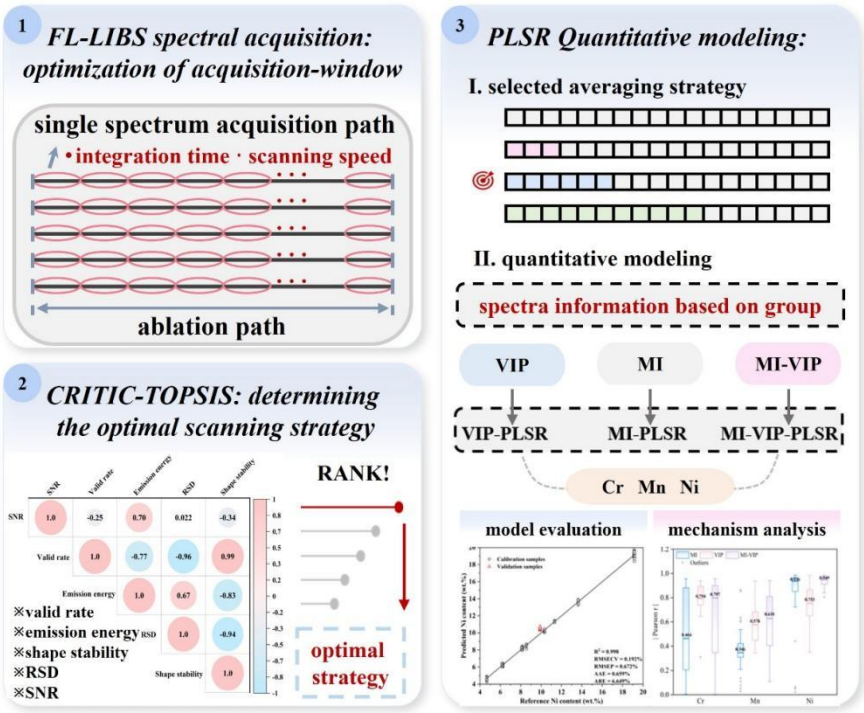

Fig. 1 Workflow for spectral acquisition-window optimization and quantitative validation of Cr, Mn, and Ni in Z3CN20-09M steel by FL-LIBS.

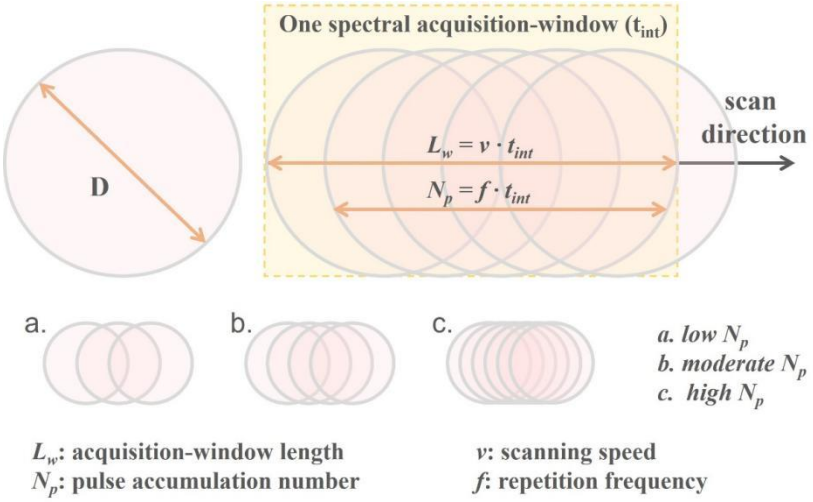

Fig. 2 Schematic illustration of the spectral acquisition-window in FL-LIBS.

described as a spectral acquisition-window. A detailed diagram is shown in Fig. 2. Two descriptors were used to characterize this window. The pulse accumulation number, N_p [1], was calculated as:

$$N_p = f * t_{int} \quad (1)$$

The acquisition-window length, L_w, was calculated as:

$$L_w = v * t_{int} \quad (2)$$

where f is the laser repetition rate, t_{int} is the spectrometer integration time, and v is the scanning speed. In this study, f was 35 kHz and the ablation spot diameter, D, was approximately 40 μm [26]. The ratio L_w / D was used to compare the surface length covered during one integration period with the laser spot diameter. Values of L_w / D below, close to, and above 1 indicate that the

acquisition-window length is smaller than, comparable to, and larger than the laser spot diameter, respectively.

Spectral preprocessing. To improve spectral quality, the acquired spectra were subjected to spectrum validity screening. The procedure was as follows. First, saturated spectra were removed. A spectrum was considered saturated when its maximum intensity exceeded the detector threshold of 60000. The remaining non-saturated spectra were then screened for weak excitation. A set of characteristic emission peaks was selected, and the local background was subtracted for each peak. The net peak areas of all selected peaks were summed to obtain the multi-peak net emission intensity, E_i, for each spectrum. For the P-th characteristic peak, the net peak area, I_{pj}, was calculated as follows:

$$I_{pj} = \sum_{i \in P_p} \left(X_{ij} - B_{pj} \right) \tag{3}$$

where P_p denotes the peak window, and B_{pj} is the median intensity of the left and right background windows of this peak. Negative net areas were set to zero. The multi-peak net emission intensity of the j-th spectrum was calculated as:

$$E_j = \sum_p I_{pj} \tag{4}$$

A robust threshold based on the median and the median absolute deviation (MAD) was then used to remove weak-excitation spectra. Let *med(E)* be the median multi-peak net intensity of all non-saturated spectra. The *MAD* was defined as:

$$MAD(E) = median\left(| E_j - med(E) | \right) \tag{5}$$

The robust standard deviation was estimated as:

$$\sigma_E = 1.4826 * MAD(E) \tag{6}$$

The threshold for weak-excitation screening was defined as:

$$T_E = max\left(med(E) - 3\sigma_E, 0.50 * med(E), 0 \right) \tag{7}$$

when $E_j < T_E$, the spectrum was classified as a weak-excitation spectrum and removed. Spectral-shape consistency screening was further performed. The median spectrum of the spectra retained after weak-excitation screening was used as the reference spectrum:

$$X_{ref} = median(X_{energy}, 2) \tag{8}$$

The Pearson correlation coefficient between each spectrum and the reference spectrum was then calculated [27]:

$$r_j = \frac{(X_j - \overline{X_j})(X_{ref} - \overline{X_{ref}})}{\sqrt{\sum_i (X_{ij} - \overline{X_j})^2} \sqrt{\sum_i (X_{ref,i} - \overline{X_{ref}})^2}} \tag{9}$$

A correlation threshold was also constructed using the median and *MAD*:

$$T_r = max(med(r) - 3 * 1.4826 * MAD(r), 0.90) \tag{10}$$

when $r_j < T_r$, the spectrum was classified as a shape-abnormal spectrum and removed. After spectral screening, channel-wise total-intensity normalization was applied to the retained valid spectra to obtain the final spectral dataset.

CRITIC-TOPSIS weighting. After spectral preprocessing, several evaluation metrics were obtained, including saturation rate, spectral-shape abnormality rate, and valid spectrum rate. To comprehensively evaluate the effects of different scanning conditions on high-frequency laser acquisition, and to avoid the subjectivity of manual weighting, the CRITIC-TOPSIS method was used for comprehensive ranking. In this procedure, CRITIC was first used to calculate the objective weights of the evaluation indicators, and TOPSIS was then applied to rank the scanning conditions [28,29].

CRITIC is an objective weighting method in which the weight of each indicator is determined by its information content. It mainly considers two aspects: the variability of each indicator and the conflict among different indicators. The evaluation matrix was first constructed as follows:

$$X = (x_{ij})_{m*n} \tag{11}$$

where m is the number of experimental conditions to be evaluated, and n is the number of evaluation indicators. Before calculation, indicators with different directions and units need to be normalized. For benefit indicators, the normalization is performed as follows:

$$z_{ij} = \frac{x_{ij} - min(x_j)}{max(x_j) - min(x_j)} \tag{12}$$

For cost indicators, the normalization is performed as follows:

$$z_{ij} = \frac{max(x_j) - x_{ij}}{max(x_j) - min(x_j)} \tag{13}$$

Where z_{ij} denotes the normalized indicator after direction unification. The standard deviation of each indicator is then calculated to represent its variability under different experimental conditions:

$$s_j = \sqrt{\frac{1}{m-1} \sum_{i=1}^{m} (z_{ij} - \overline{z_j})^2} \tag{14}$$

Meanwhile, the correlation coefficient r_{jk} between indicators is calculated to represent the degree of information overlap among them. Therefore, the information content of the j-th indicator is

defined as:

$$C_j = s_j \sum_{k=1}^{n} (1 - r_{jk}) \tag{15}$$

Finally, the weight of each indicator is calculated as:

$$\omega_j = \frac{C_j}{\sum_{j=1}^{n} C_j} \tag{16}$$

After obtaining the weights of all indicators, the TOPSIS method was further used to calculate the closeness of each scanning condition to the ideal solution [30]. The basic principle of TOPSIS is that the optimal experimental condition should be as close as possible to the positive ideal solution and as far as possible from the negative ideal solution. First, the weighted normalized matrix was constructed using the CRITIC weights [31]:

$$v_{ij} = \omega_j z_{ij} \tag{17}$$

The positive ideal solution and the negative ideal solution were then determined as follows:

$$A^{+} = \left\{ max(n_{ij}) \right\} \tag{18}$$

$$A^{-} = \left\{ min(n_{ij}) \right\} \tag{19}$$

The Euclidean distances between the *i*-th experimental condition and the positive and negative ideal solutions were then calculated:

$$D_i^{+} = \sqrt{\sum_{j=1}^{n} (v_{ij} - A_j^{+})^2} \tag{20}$$

$$D_i^{+} = \sqrt{\sum_{j=1}^{n} (v_{ij} - A_j^{-})^2} \tag{21}$$

Finally, the closeness coefficient was calculated:

$$CC_i = \frac{D_i^{-}}{D_i^{+} + D_I^{-}} \tag{22}$$

where CC_j value indicates that the experimental condition is closer to the optimal condition and has better overall spectral quality.

Feature extraction methods. Three feature extraction strategies, namely MI, VIP, and the combined MI-VIP method, were used to identify spectral variables for elemental prediction. The procedure was performed separately for Cr, Mn, and Ni. The preprocessed LIBS spectra contained 4096 spectral variables. These variables included redundant information and strong collinearity among adjacent channels. Direct use of the full-spectrum matrix may reduce model robustness and increase computational complexity. Therefore, feature extraction was introduced before PLSR modeling to retain element-related variables and remove weakly informative spectral.

MI was used as a filter-based variable-selection method to quantify the statistical dependence between each spectral variable and the concentration of a target element [32,33]. MI scores were calculated separately for Cr, Mn, and Ni, and all spectral variables were ranked in descending order. Variables with higher MI scores were retained as candidate features for subsequent PLSR modeling.

VIP was used as a model-based variable-selection method. For each target element, an initial PLSR model was constructed, and the number of latent variables was determined by cross-validation using the calibration set. VIP scores were then calculated to evaluate the contribution of each spectral variable to the PLSR model. The variables were ranked according to their VIP scores, and those with higher scores were retained for subsequent modeling [34,35].

The MI-VIP strategy combined the complementary roles of MI and VIP. MI was first used to remove variables with weak concentration relevance and generate a reduced candidate subset. VIP was then applied within this subset to identify variables that made stronger contributions to the PLSR model. This two-step procedure was performed separately for Cr, Mn, and Ni. All three methods used standard-sample leave-one-out cross-validation (LOSO-CV) within the calibration set to optimize the numbers of retained variables and PLS components, with RMSE used as the selection criterion. For MI-VIP, models within 1% of the minimum RMSE were considered comparable and the simpler model was retained.

PLSR model. PLSR projects high-dimensional spectral variables onto a small number of latent variables, while maximizing the covariance between spectral data and target concentrations.[36,37] This makes it suitable for LIBS spectra, where numerous emission lines, spectral overlap, and matrix effects often lead to strong correlations among spectral variables. Separate PLSR models were developed for Cr, Mn, and Ni using the preprocessed spectral data. The number of retained variables, where applicable, and the number of PLS components were optimized by cross-validation using the calibration set. Model performance was evaluated using the coefficient of determination R^2, root mean square error of cross-validation (RMSECV), root mean square error of prediction (RMSEP), average absolute error (AAE), and average relative error (ARE). All feature-selection and model-optimization procedures were performed using the calibration set. All MI calculation, VIP computation, and PLSR parameter optimization were performed solely using the calibration set. The Z3CN20-09M spectra were used only for external prediction after the final models had been established.

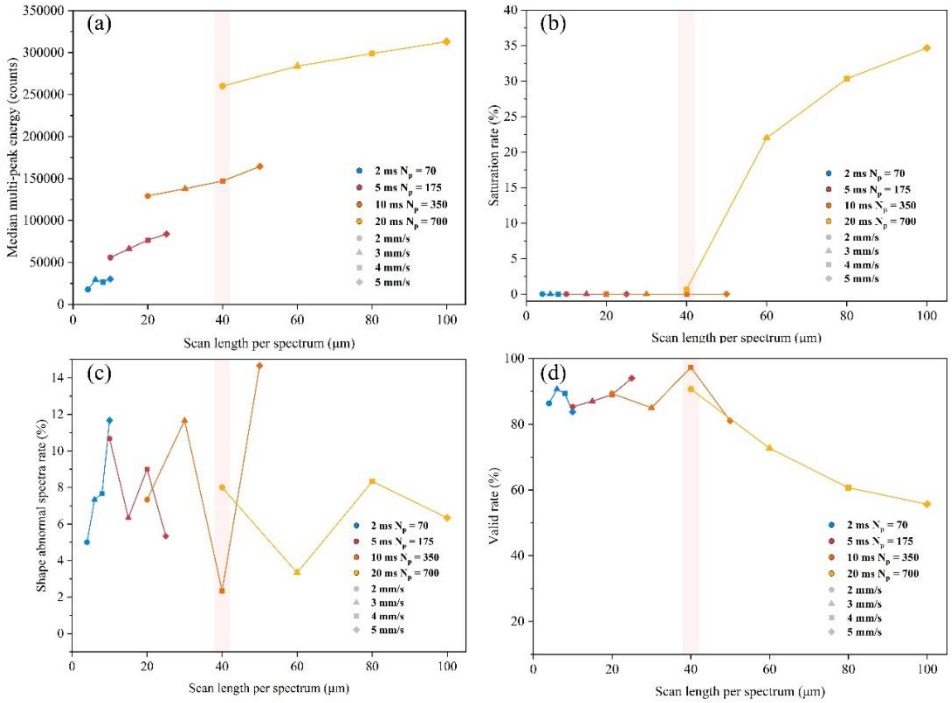

Fig. 3 Effects of the spectral acquisition-window length (L_w) and pulse accumulation number (N_p) on FL-LIBS spectral quality: (a) median multi-peak energy, (b) saturation rate, (c) shape-abnormal spectra rate, and (d) valid rate.

Table 2. Scanning conditions and spectral acquisition-window descriptors

No.	Integration time (ms)	Scanning speed (mm s^{-1})	N_p	L_w (μm)
1	2	2	70	4
2	2	3	70	6
3	2	4	70	8
4	2	5	70	10
5	5	2	175	10
6	5	3	175	15
7	5	4	175	20
8	5	5	175	25
9	10	2	350	20
10	10	3	350	30
11	10	4	350	40
12	10	5	350	50
13	20	2	700	40
14	20	3	700	60
15	20	4	700	80
16	20	5	700	100

RESULTS AND DISCUSSION

Spectral acquisition-window analysis of scanning conditions in FL-LIBS. Sixteen scanning conditions were evaluated to determine how the temporal and spatial extent of a spectral acquisition-window affects FL-LIBS spectral quality. The four integration times and four scanning speeds generated the paired N_p and L_w conditions listed in Table 2. Conditions with the same L_w can differ in spectral stability.

For each condition, 300 spectra were collected. Fig. 3 summarizes the median multi-peak emission energy, saturation rate, spectral-shape abnormality rate, and valid-spectrum rate as functions of acquisition-window length L_w and pulse accumulation number N_p. At 2 ms, each spectrum contained only 70 pulses and covered 4-10 μm, far less than the 40 μm laser spot diameter. Although saturation was absent, these conditions gave the lowest median multi-peak emission energies, indicating insufficient signal accumulation within a single spectrum. Median emission energy increased with N_p and L_w, but this increase did not lead to a monotonic improvement in spectral quality. At 20 ms, N_p reached 700, and saturation became more prevalent as L_w increased. The 5 and 10 ms conditions instead provided a more favorable balance between emission intensity and spectral stability. The comparison at L_w=40 further isolated the effect of pulse accumulation. Although the two conditions covered a surface length comparable to the laser spot diameter, the condition with N_p=350 showed a lower spectral-shape abnormality rate and a higher valid-spectrum rate than that with N_p=700. Thus, matching L_w to the laser spot diameter alone was insufficient; both L_w and N_p needed to be balanced to obtain stable and representative spectra. Accordingly, the 2 and 20 ms conditions were excluded from subsequent comparison, whereas the 5 and 10 ms conditions were retained as candidate conditions.

In LIBS quantitative analysis, the reliability of model input

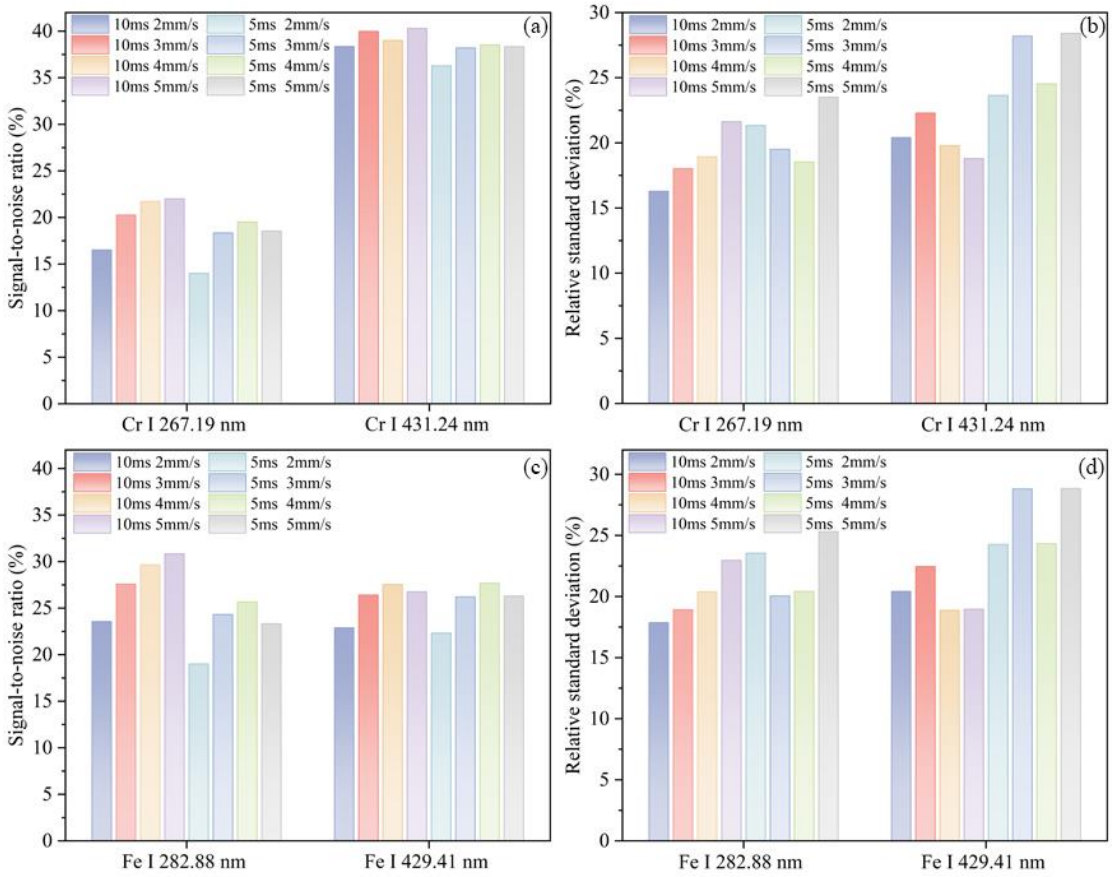

Fig. 4 Analysis of representative spectral quality under different parameter conditions. (a), (c): SNR and (b), (d): RSD.

Table 3. The parameters of analysis lines

Spectral line	Wavelength (nm)	g_kA_{ki} (s^{-1})	E_i (eV)	E_k (eV)
Cr I	267.19	6.00e+07	0.97	5.60
Fe I	282.88	1.31e+07	0.99	5.37
Fe I	429.41	2.81e+07	1.48	4.37
Cr I	431.24	1.50e+07	3.11	5.99

variables depend on both signal intensity and spectral stability. The signal-to-noise ratio (SNR) reflects how clearly characteristic emission lines can be distinguished from the local background. A higher SNR indicates a stronger analytical signal, which is beneficial for weak-line identification and quantitative modeling. The relative standard deviation (RSD) describes the fluctuation ofpeak intensity across repeated spectra. A lower RSD indicates better spectral repeatability and more stable model inputs. Based on the acquisition-window analysis above, the 5 and 10 ms conditions were further examined using representative emission lines, because these conditions showed zero saturation and relatively high valid spectrum rates. Four representative emission lines were selected for comparison: Cr I 267.19 nm, Cr I 431.24 nm, Fe I 282.88 nm, and Fe I 429.41 nm. Their SNR and RSD values were used to evaluate the effect of scanning parameters on characteristic line quality. Detailed information on these emission lines is provided in Table 3.

Figure 4 compares the SNR and RSD values of four representative emission lines under the 5 and 10 ms conditions. The SNR depended on both the emission line and the scanning speed. For the relatively weak or strongly interfered Cr I 267.19 nm and Fe I 282.88 nm lines, the 10 ms condition generally produced higher SNR values than the 5 ms condition. At a given integration time, increasing the scanning speed from 2 to 5 mm s^{-1} was also associated with higher SNR values. In contrast, the stronger Cr I 431.24 nm and Fe I 429.41 nm lines maintained high SNR values under both integration times, with only small differences between conditions. Thus, within the tested range, the longer integration time was particularly beneficial for the weaker or interference-sensitive lines. The RSD results showed a different pattern. For Cr I 267.19 nm and Fe I 282.88 nm, the 10 ms condition generally yielded lower RSD values at scanning speeds of 2-4 mm s^{-1}, whereas the 5 ms condition showed greater speed-dependent fluctuations. For Cr I 431.24 nm and Fe I 429.41 nm, several 10 ms conditions gave slightly higher RSD values, indicating that increased signal intensity did not uniformly improve repeatability. Overall, the 10 ms condition provided higher or comparable SNR values and more favorable stability for

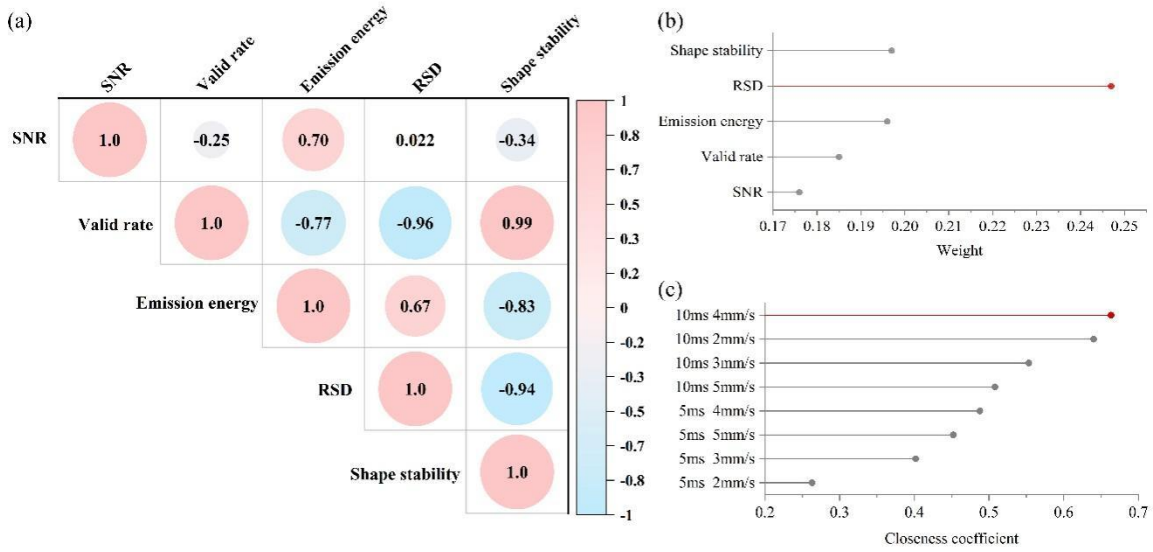

Fig. 5 CRITIC-TOPSIS-based comprehensive evaluation of scanning parameters under the 5 and 10 ms conditions. (a) Correlation matrix of the evaluation indicators, (b) CRITIC weights of the indicators, and (c) TOPSIS closeness coefficients of different scanning parameter settings.

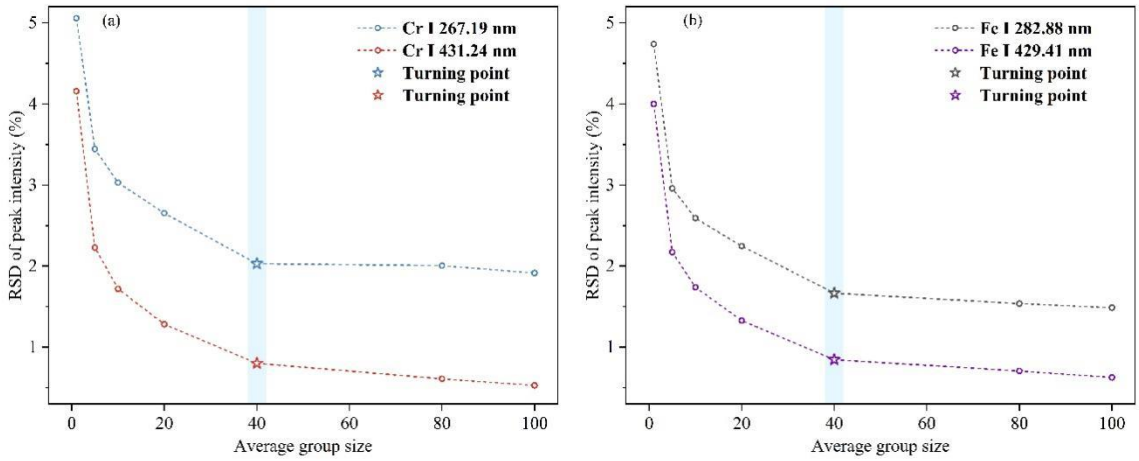

Fig. 6 Effect of spectral averaging number on the RSD of peak intensity for representative emission lines: (a) Cr and (b) Fe.

the analytically challenging lines. The 5 ms condition, however, avoided saturation and maintained a high valid-spectrum rate. Because no single metric captured both analytical signal and spectral stability, the 5 and 10 ms candidate conditions were ranked using CRITIC-TOPSIS to reduce the subjectivity of manual weighting. The results are shown in Fig. 5. Fig. 5(a) shows the correlations among the evaluation indicators. Some indicators were strongly correlated. For example, valid spectrum rate was positively correlated with shape stability, but negatively correlated with RSD, indicating information overlaps among these stability-related indicators. In contrast, SNR and emission energy showed different correlation patterns from the stability indicators. This further supports the need for a multi-indicator evaluation. The CRITIC weights are shown in Fig. 5(b). RSD had the highest weight, indicating that spectral repeatability contributed most to the comprehensive evaluation. Shape stability, emission energy, valid spectrum rate, and SNR also contributed to the final ranking. According to the TOPSIS closeness coefficient, the 10 ms conditions performed better than the 5 ms conditions. Within this candidate set, 10 ms and 4 mm s^{-1} gave the highest TOPSIS closeness coefficient and was selected as the working condition for subsequent quantitative validation.

Calibration models for Z3CN20-09M quantitative analysis. ***Effect of group averaging on spectral stability.*** After the scanning condition had been selected, 400 valid spectra were retained for each certified reference material and the Z3CN20-09M sample. The number of spectra per averaging group was then optimized to reduce spectral fluctuations while preserving sufficient groups for subsequent modeling [38]. Because RSD had the largest CRITIC weight in Fig. 5, it was used as the primary stability indicator. The

RSDs of peak intensities for four representative Cr and Fe emission lines were evaluated at averaging group sizes of 1, 5, 10, 20, 40, 80, and 100 spectra.

The results are shown in Fig. 6. As the averaging number increased, the RSD values of all four emission lines decreased.The decrease was rapid from 1 to 40 averaged spectra, but became much smaller when the averaging number increased to 80 or 100. This indicates that 40 averaged spectra marked a practical turning point in spectral stability improvement. Below this value, increasing the averaging number substantially improved spectral repeatability. Beyond this value, further averaging gave only limited RSD reduction, while decreasing the number of groups available for modeling and prediction. Therefore, considering peak-intensity stability, sample number, and the requirements of subsequent prediction, 40 spectra were selected as one averaging group.

Quantitative validation of the spectral acquisition-window optimization. To directly verify whether the spectral acquisition-window optimization improved quantitative performance, full-spectrum PLSR models were established under three representative scanning conditions: 10 ms at 2 mm s^{-1} (N_p=*350, L_w=20*), 20 ms at 2 mm s^{-1} (N_p=*700, L_w=40*), and 10 ms at 4 mm s^{-1} (N_p=*350, L_w=40*). The first and third conditions had the same pulse accumulation number but different acquisition-window lengths, allowing the effect of surface coverage per spectrum to be evaluated. The second and third conditions had the same acquisition-window length but different pulse accumulation numbers, allowing the influence of pulse accumulation to be examined independently. All spectra were subjected to the same validity screening, normalization, group-averaging strategy, calibration procedure, and cross-validation protocol. Full-spectrum PLSR was used as a common baseline to avoid confounding the comparison with differences in variable-selection methods. The Z3CN20-09M specimen was excluded from model development and used only for external validation. Therefore, differences in model performance could be attributed primarily to the spectral acquisition-window condition.

Fig. 7 compares the quantitative results obtained under the three acquisition-window conditions. The 10 ms-4 mm s^{-1} condition consistently provided the best calibration and external-validation performance for Cr, Mn, and Ni. For Cr, the model obtained under this condition achieved an R^2 of 0.955 and an RMSECV of 0.702

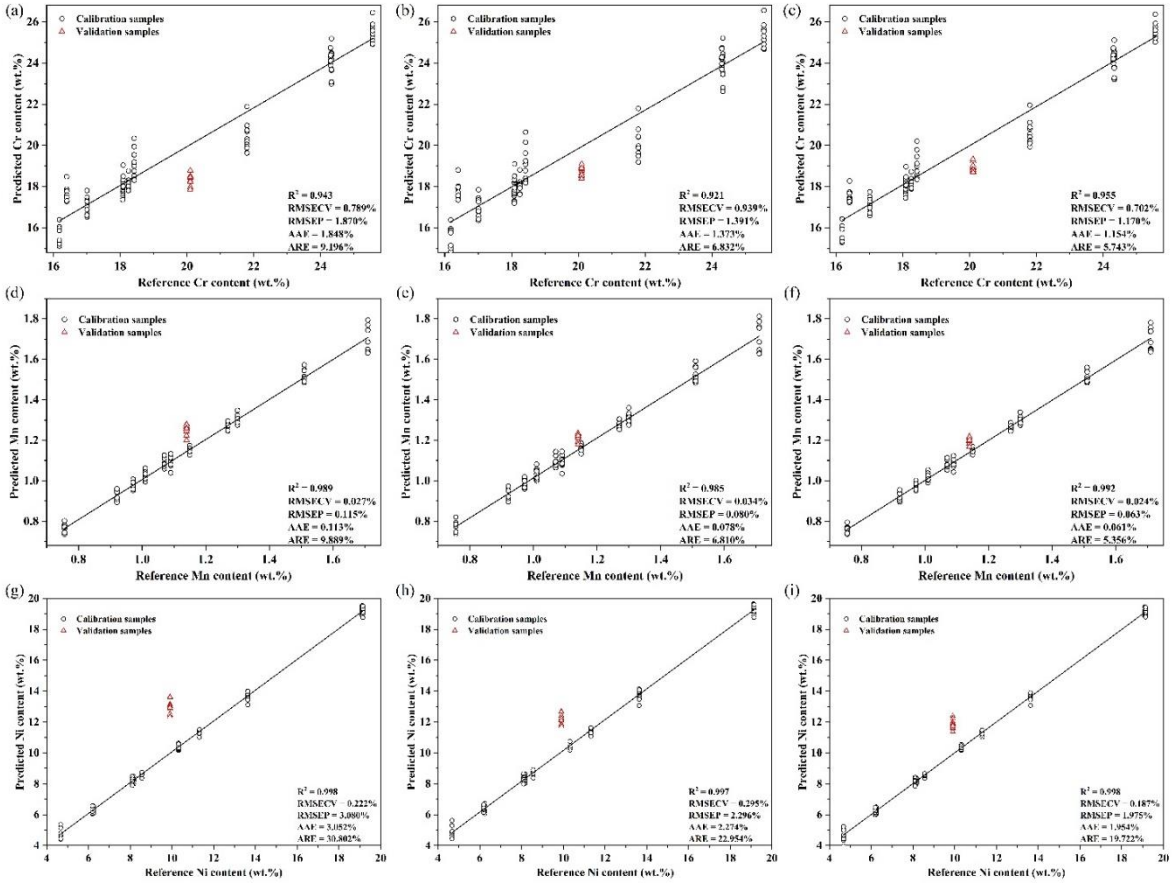

Fig. 7 Full-spectrum PLSR results for Cr, Mn, and Ni obtained under three representative spectral acquisition-window conditions: (a), (d), and (g) 10 ms at 2 mm s^{-1} (N_p=*350, L_w=20*); (b), (e), and (h) 20 ms at 2 mm s^{-1} (N_p=*700, L_w=40*); and (c), (f), and (i) 10 ms at 4 mm s^{-1} (N_p=*350, L_w=40*).

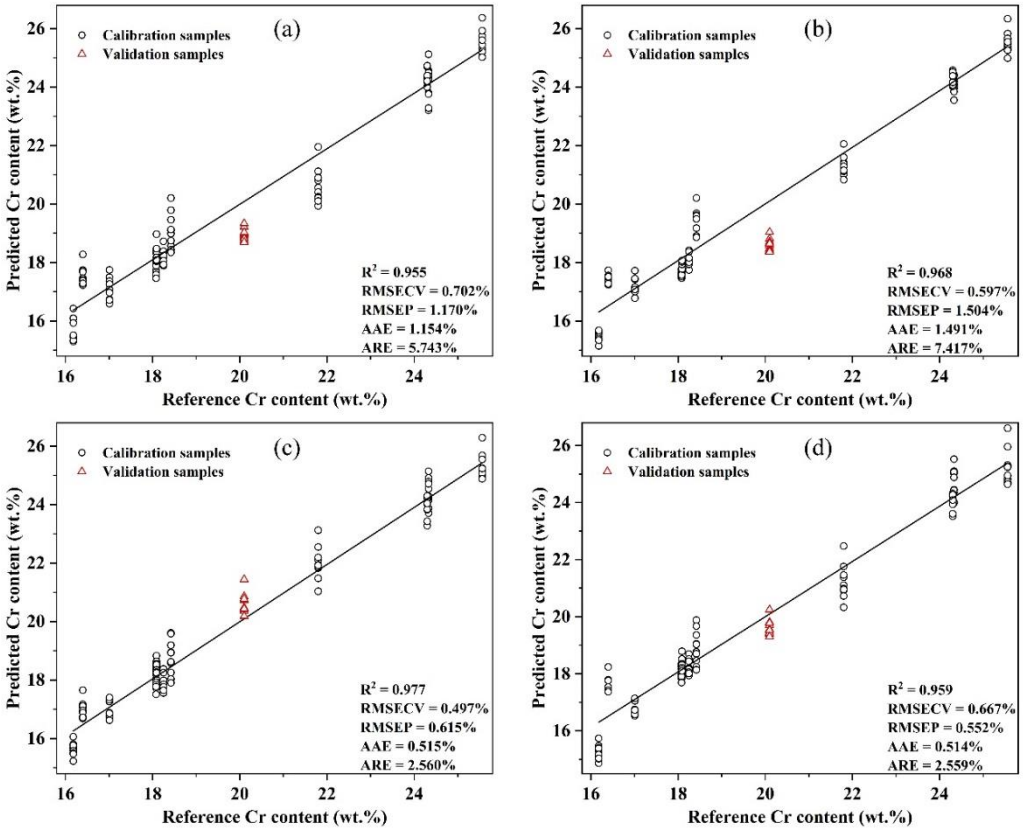

Fig. 8 Quantitative prediction results for Cr obtained using different PLSR-based models: (a) full-spectrum PLSR, (b) VIP-PLSR, (c) MI-PLSR, and (d) MI-VIP-PLSR.

wt.%, together with an RMSEP, AAE, and ARE of 1.170 wt.%,1.154 wt.%, and 5.743%, respectively. The corresponding values for Mn were 0.992, 0.024 wt.%, 0.063 wt.%, 0.061 wt.%, and 5.356%, while those for Ni were 0.998, 0.187 wt.%, 1.975 wt.%, 1.954 wt.%, and 19.722%, respectively. At a fixed pulse accumulation number of N_p=*350*, increasing the acquisition-window length from 20 to 40 μm reduced the RMSEP values by 37.4% for Cr, 45.2% for Mn, and 35.9% for Ni. This result indicates that the shorter 20 μm acquisition window did not provide sufficiently representative surface sampling during each spectral integration period. At a fixed acquisition-window length of L_w=*40*, reducing the pulse accumulation number from 700 to 350 further decreased the RMSEP values by 15.9%, 21.3%, and 14.0% for Cr, Mn, and Ni, respectively. These results indicate that increasing pulse accumulation alone did not improve quantitative performance. Instead, the 10 ms-4 mm s^{-1} condition provided a more favorable balance between signal accumulation, spectral stability, and surface representativeness. The quantitative comparison therefore validates the spectral-quality-based optimization and demonstrates that an acquisition-window close to the laser spot diameter is more suitable for robust FL-LIBS quantification of alloying elements.

Quantitative model optimization under the selected acquisition-window. After the selected acquisition-window had been quantitatively validated, the subsequent analysis focused on further improving the quantitative performance for Cr, Mn, and Ni. Spectra acquired at 10 ms and 4 mm s^{-1} (N_p=*350*, L_w=*40*) were used to construct PLSR models. Full-spectrum PLSR was first established as the baseline, and variable-selection strategies based on VIP, MI, and their combination were subsequently introduced to reduce redundant spectral information and optimize prediction accuracy.

Fig. 8 shows the Cr prediction results obtained using full-spectrum PLSR, VIP-PLSR, MI-PLSR, and MI-VIP-PLSR. For the calibration samples, all four models produced predicted values close to the fitted regression line, indicating that the main Cr-related spectral variation was captured during calibration. In the prediction of the independent blind Z3CN20-09M sample, however, the four models showed clear differences in prediction bias and error. The full-spectrum PLSR model achieved an R^2 of 0.955 and an RMSECV of 0.702 wt.%, but it underestimated the Cr content of the blind sample. The corresponding RMSEP and ARE were 1.170 wt.% and 5.743%, respectively. VIP-PLSR improved the calibration result, with an R^2 of 0.968 and an

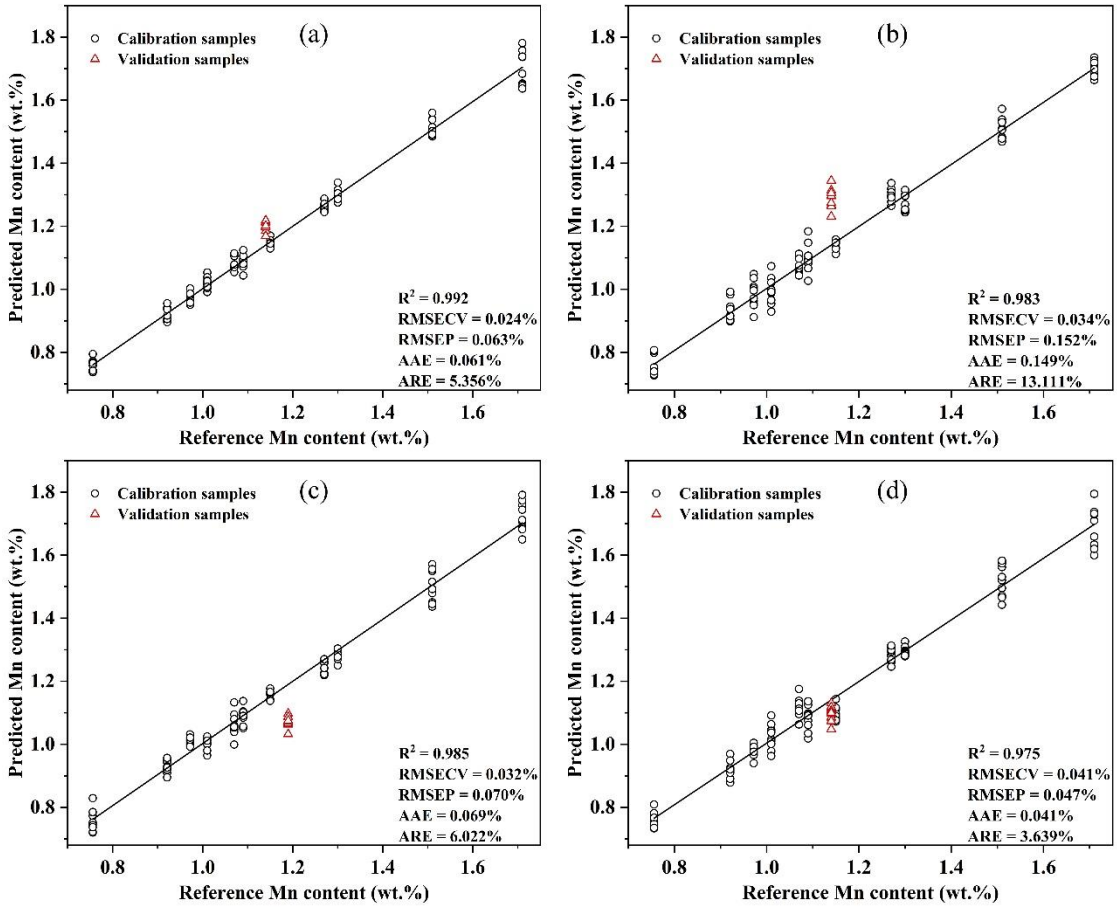

Fig. 9 Quantitative prediction results for Mn obtained using different PLSR-based models: (a) full-spectrum PLSR, (b) VIP-PLSR, (c) MI-PLSR, and (d) MI-VIP-PLSR.

RMSECV of 0.597 wt.%. However, its external prediction error increased to an RMSEP of 1.504 wt.% and an ARE of 7.417%. This suggests that VIP-selected variables were effective for calibration but not fully transferable to the Z3CN20-09M matrix. In contrast, MI-PLSR markedly reduced the prediction error for the blind sample, with an RMSEP of 0.615 wt.% and an ARE of 2.560%. The proposed MI-VIP-PLSR model further reduced the RMSEP to 0.552 wt.%, with a comparable ARE of 2.559%. These results indicate that MI-VIP improved external prediction robustness by combining relevance screening with latent-variable contribution evaluation. This reduced the influence of redundant and matrix-specific spectral information.

Fig. 9 presents the Mn prediction results obtained using the four PLSR-based models. Compared with Cr and Ni, Mn was present at a lower concentration level, making its prediction more sensitive to matrix interference and spectral fluctuation. The full-spectrum PLSR model showed the best calibration performance, with an R^2 of 0.992 and an RMSECV of 0.024 wt.%. However, its prediction error for the independent blind Z3CN20-09M sample remained evident, with an RMSEP of 0.063 wt.% and an ARE of 5.356%. VIP-PLSR showed the poorest external prediction performance, with an RMSEP of 0.152 wt.% and an ARE of 13.111%. This suggests that VIP selection alone was insufficient to retain weak and interference-sensitive Mn-related information. MI-PLSR improved the prediction accuracy compared with VIP-PLSR, reducing the ARE to 6.022%. In contrast, MI-VIP-PLSR achieved the lowest blind-sample prediction error, with an RMSEP of 0.047 wt.%, an AAE of 0.041 wt.%, and an ARE of 3.639%, although its calibration R^2 and RMSECV were not the best among the four models.

Fig. 10 shows the Ni prediction results obtained using the four PLSR-based models. All models showed strong calibration performance, with R^2 values of 0.998 or higher. This indicates that the Ni-related spectral response was well fitted by PLSR. However, their external prediction performances differed considerably. The full-spectrum PLSR model showed a large positive deviation for the independent blind Z3CN20-09M sample, with an RMSEP of 1.975 wt.%, an AAE of 1.954 wt.%, and an ARE of 19.722%, despite its high calibration R^2. After feature selection, the prediction error was markedly reduced. VIP-PLSR and MI-PLSR

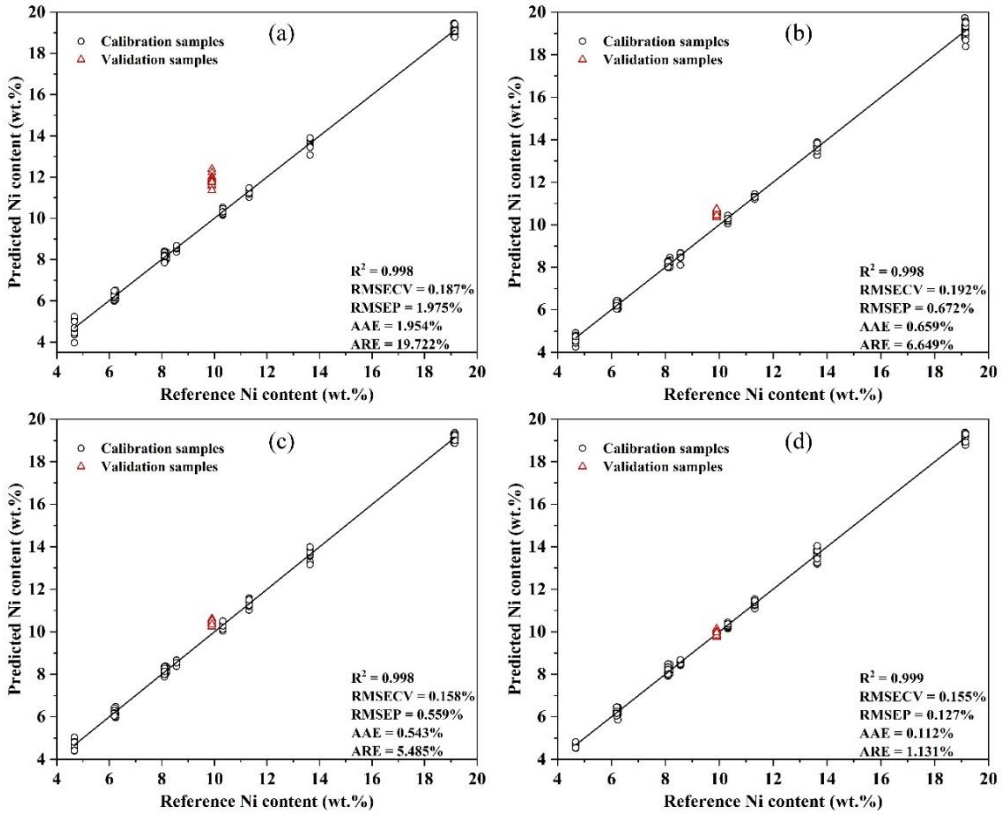

Fig. 10 Quantitative prediction results for Ni obtained using different PLSR-based models: (a) full-spectrum PLSR, (b) VIP-PLSR, (c) MI-PLSR, and (d) MI-VIP-PLSR.

Table 4. Precision comparison of MI-VIP-PLSR prediction results with the national standard limits[2][3]

Element	Reference	Predicted results			r	R	max $\lvert x_i - x_j \rvert$
Cr	20.10	19.696	19.802	19.548	0.271	0.383	0.254
Mn	1.140	1.084	1.073	1.097	0.025	0.048	0.024
Ni	9.907	10.081	10.015	10.145	0.134	0.257	0.130

decreased the ARE to 6.649% and 5.485%, respectively. This suggests that feature selection removed part of the redundant and matrix-related spectral information. The proposed MI-VIP-PLSR model achieved the best overall performance, with an R^2 of 0.999, an RMSECV of 0.155 wt.%, an RMSEP of 0.127 wt.%, an AAE of 0.112 wt.%, and an ARE of 1.131%. This demonstrates that the MI-VIP strategy substantially improved the transferability and robustness of the Ni calibration model.

After the model comparison, the precision of the selected MI-VIP-PLSR method was evaluated according to the relevant national standard GB/T 11170-2008 [39]. According to this standard, the absolute difference between two independent results should not exceed the repeatability limit, r , under repeatability conditions, or the reproducibility limit, R , under reproducibility conditions. For this purpose, three independent prediction results were obtained for the Z3CN20-09M sample. The maximum pairwise difference, max $\lvert x_i - x_j \rvert$, was then used for comparison according to the standard precision criterion, and the results are summarized in Table 4. For Cr, Mn, and Ni, the maximum differences were 0.254, 0.024, and 0.130 wt.%, respectively. These values were lower than the corresponding repeatability limits of 0.271, 0.025, and 0.134 wt.%, and lower than the reproducibility limits of 0.383, 0.048, and 0.257 wt.%. These results show that the optimized FL-LIBS method satisfied the national-standard precision requirements for Cr, Mn, and Ni. The standard comparison therefore provides application-oriented support for the repeatability of the optimized FL-LIBS workflow.

Interpretation of selected spectral variables. To examine how feature extraction affected the spectral information used for modeling, the selected variables were mapped onto the average LIBS spectrum. Fig. 11 shows the variables selected by MI, VIP, and MI-VIP. MI selected variables across a broad spectral range,

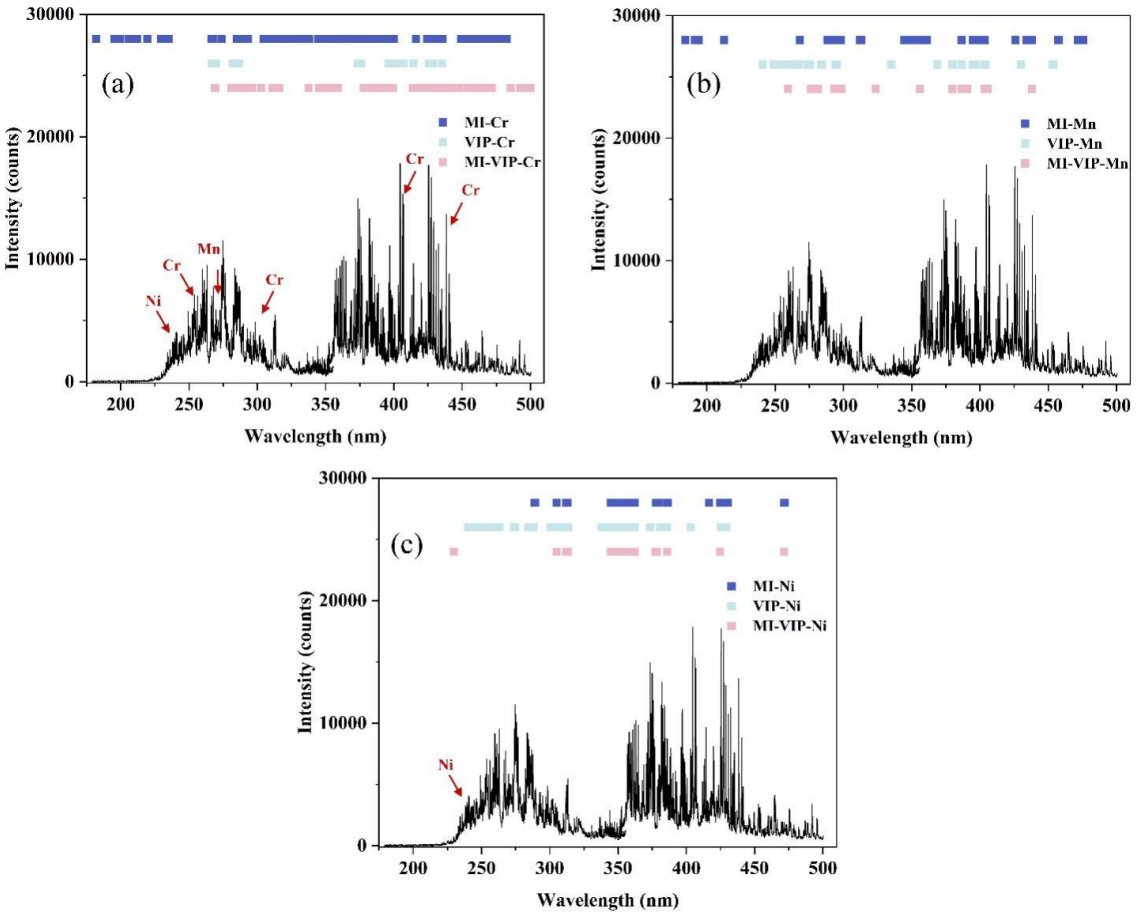

Fig. 11 Distribution of variables selected by MI, VIP, and MI-VIP for the quantitative analysis of (a) Cr, (b) Mn, and (c) Ni.

Table 5. Number of selected variables and PLS components used in the PLSR models for Cr, Mn, and Ni

Element	Method	Number of selected variables	PLS components
Cr	MI	160	4
Cr	VIP	30	4
Cr	MI-VIP	150	2
Mn	MI	50	7
Mn	VIP	50	7
Mn	MI-VIP	20	4
Ni	MI	50	9
Ni	VIP	111	9
Ni	MI-VIP	50	8

especially in emission-rich regions. VIP retained fewer variables, mainly in localized regions related to the PLS latent-variable structure. MI-VIP showed a more compact and complementary distribution. This indicates that the two-step strategy reshaped the variable space for PLSR modeling, rather than simply reproducing the VIP-selected features.

Table 5 summarizes the number of selected variables and the corresponding PLS components. Compared with MI or VIP alone, MI-VIP generally reduced both values. This indicates a simpler model structure. The compact feature subsets still covered target-element lines, Fe matrix lines, and partially overlapped regions. For Cr, several MI-VIP variables fell outside the final MI- and VIP-only subsets because VIP screening was performed within a broader MI candidate set, whereas the greater overlap observed for Mn and Ni reflected their independently optimized subset sizes. These variables may preserve both elemental response and matrix-correction information.

The analysis above described the location and number of variables selected by different feature extraction strategies. To further assess their concentration relevance, the absolute Pearson correlation coefficients between the selected variables and target-element concentrations were calculated, as shown in Fig. 12. MI showed broad $|r|$ distributions, with median values of 0.464, 0.346, and 0.936 for Cr, Mn, and Ni, respectively. VIP increased the median $|Pearson\,r|$ values for Cr and Mn to 0.794 and 0.578, respectively, but showed a lower median value for Ni than MI. This indicates that variables with high PLSR contribution were not always those most directly correlated with elemental concentration. In contrast, MI-VIP achieved median $|Pearson\,r|$

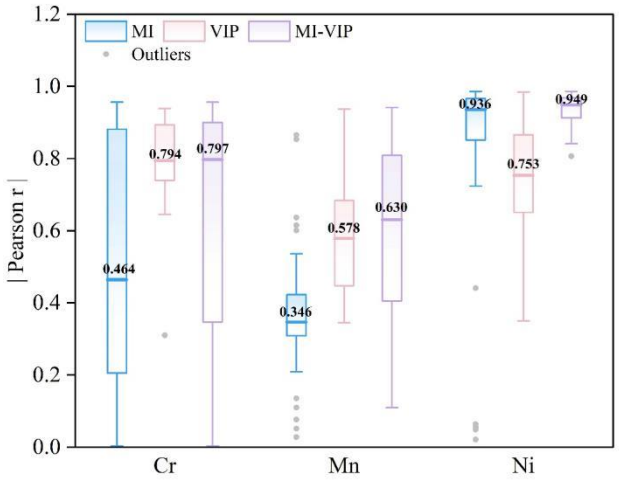

Fig. 12 Distribution of Pearson correlations between variables and target element concentrations, as screened using different feature selection methods.

values of 0.797, 0.630, and 0.949 for Cr, Mn, and Ni, respectively. These were the highest values among the three methods for all target elements. Thus, MI-VIP not only retained variables with strong concentration relevance, but also incorporated their contribution to PLSR modeling. This dual selection mechanism improved the chemical relevance of the selected variables while maintaining their modeling effectiveness.

CONCLUSION

This study developed a spectral acquisition-window optimization strategy for FL-LIBS quantification of Cr, Mn, and Ni in Z3CN20-09M steel. The acquisition window was defined by pulse accumulation number N_p and acquisition-window length L_w, which represent temporal emission accumulation and spatial surface coverage during one spectral integration period. Spectral-quality analysis and CRITIC-TOPSIS identified 10 ms at 4 mm s^{-1} as the selected condition. At this setting, L_w was 40 μm, approximately matching the laser spot diameter, and N_p was 350. A matched three-condition PLSR comparison further validated this selection. At a fixed N_p, increasing L_w from 20 to 40 μm improved quantitative performance, whereas, at a fixed L_w of 40 μm, increasing N_p from 350 to 700 provided no further benefit. These findings confirm that reliable FL-LIBS quantification requires a balance between pulse accumulation and surface coverage. Under the selected acquisition window, MI-VIP-PLSR further improved the quantitative results, achieving RMSEPs of 0.552, 0.047, and 0.127 wt.% for Cr, Mn, and Ni, respectively. The predictions also satisfied the precision requirements of GB/T 11170-2008. Within the calibration range examined here, the proposed strategy provides a physically interpretable basis for selecting FL-LIBS parameters and supports rapid, reliable quantification of alloying elements in steel.

AUTHOR INFORMATION

Shunchun Yao received his Bachelor's in 2006 from the Soochow University, China, and PhD in 2011 from the school of Electric power, South China University of Technology (SCUT). He is a research professor of power engineering and engineering thermos-physics at the School of Electric Power, SCUT. His major research interests are intelligent sensing and regulation research of energy conversion process. He was selected as one of the national high-level young talents, and is the current director of the Key Laboratory of Efficient and Clean Utilization of Energy in Guangdong Province, deputy director of the Engineering Research Center for High-Efficiency and Low-Pollution Energy Conversion in Guangdong Province, and a LIBS Young Scientist of the Optical Engineering Society of China. He is author or co-author of over 100 articles published in peer-reviewed scientific journals, with an h-index of 20 (Scopus). His work is supported by the Key Program of the National Natural Science Foundation of China (NSFC).

Corresponding author

* S. C. Yao

Email address: epscyao@scut.edu.cn

Notes

The authors declare no competing financial interest.

ACKNOWLEDGMENTS

This work was financially supported by the National Natural Science Foundation of China (22B20119, 22403032, and 22573035), and the Fundamental Research Funds for the Central Universities (2025ZYGXZR025).

REFERENCES

1. T.S. Byun, Y. Yang, N.R. Overman, and J.T. Busby, *JOM*, 2016, **68**, 507–516. https://doi.org/10.1007/s11837-015-1709-9
2. W. Yu, D. Yu, H. Gao, F. Xue, and X. Chen, *J. Mater. Eng. Perform.*, 2017, **26**, 4442–4449. https://doi.org/10.1007/s11665-017-2882-5

3. N. Shirai, T. Hozumi, Y. Toh, and M. Ebihara, *J. Radioanal. Nucl. Chem.*, 2020, **325**, 949–957. https://doi.org/10.1007/s10967-020-07273-8
4. T. Yamane and M. Aimoto, *Tetsu To Hagane*, 2014, **100**, 832–845. https://doi.org/10.2355/tetsutohagane.100.832
5. A. Franciscono and S. Rollet, *Steel Res. Int.*, 2021, **92**, 2000537. https://doi.org/10.1002/srin.202000537
6. Z. Zhou, K. Zhou, X. Hou, and H. Luo, *Appl. Spectrosc. Rev.*, 2005, **40**, 165–185. https://doi.org/10.1081/ASR-200052001
7. M. Biezma, U. Martin, P. Linhardt, J. Ress, C. Rodriguez, and D. M. Bastidas, *Eng. Fail. Anal.*, 2021, **122**, 105227. https://doi.org/10.1016/j.engfailanal.2021.105227
8. R.S. Harmon and G.S. Senesi, *Appl. Geochem.*, 2021, **128**, 104929. https://doi.org/10.1016/j.apgeochem.2021.104929
9. Z. Wang, Y. Deguchi, Z. Zhang, Z. Wang, X. Zeng, and J. Yan, *Front. Phys.*, 2016, **11**, 114213. https://doi.org/10.1007/s11467-016-0607-0
10. A.S. Luna, F.B. Gonzaga, W.F.C. da Rocha, and I.C.A. Lima, *Spectrochim. Acta B*, 2018, **139**, 20–26. https://doi.org/10.1016/j.sab.2017.10.016
11. Z. Wang, Y. Chu, F. Chen, Z. Sheng, and L. Guo, *Appl. Opt.*, 2019, **58**, 7615–7620. https://doi.org/10.1364/AO.58.007615
12. Y. Zhang, C. Sun, L. Gao, Z. Yue, S. Shabbir, W. Xu, M. Wu, and J. Yu, *Spectrochim. Acta B*, 2020, **166**, 105802. https://doi.org/10.1016/j.sab.2020.105802
13. Q. Zeng, F. Deng, Z. Zhu, Y. Tang, B. Wang, Y. Xiao, L. Xiong, H. Yu, L. Guo, and X. Li, *Plasma Sci. Technol.*, 2018, **21**, 034006. https://doi.org/10.1088/2058-6272/aadede
14. Z. Lin, N. Zhang, Z. Xu, J. Liao, H. Yuan, E. Chenshen, J. Liu, J. Li, N. Zhao, and Q. Zhang, *J. Anal. At. Spectrom.*, 2022, **37**, 2082–2088. https://doi.org/10.1039/d2ja00200k
15. C. Lv, N. Zhang, Z. Lin, T. Ou, J. Li, N. Zhao, X. Yang, Q. Ma, L. Guo, and Q. Zhang, *J. Laser Appl.*, 2023, **35**, 012021. https://doi.org/10.2351/7.0000939
16. M. Scharun, C. Fricke-Begemann, and R. Noll, *Spectrochim. Acta B*, 2013, **87**, 198–207. https://doi.org/10.1016/j.sab.2013.05.007
17. Z. Xu, B. Xu, X. Peng, Y. Qin, X. Yan, X. Liao, N. Zhang, Q. Lai, J. Li, and Q. Zhang, *J. Anal. At. Spectrom.*, 2021, **36**, 2501–2508. https://doi.org/10.1039/d1ja00188d
18. D. Qu, G. Yang, X. Jin, G. Chen, Z. Bai, C. Li, and D. Tian, *Spectrochim. Acta B*, 2024, **209**, 106794. https://doi.org/10.1016/j.sab.2023.106794
19. D. Qu, B. Su, Z. Bai, B. Liu, X. Jin, G. Chen, Y. Fu, T. Gu, G. Yang, and Q. Li, *J. Anal. At. Spectrom.*, 2024, **40**, 162–172. https://doi.org/10.1039/d4ja00298a
20. F. Poggialini, B. Campanella, S. Legnaioli, S. Pagnotta, S. Raneri, and V. Palleschi, *Rev. Sci. Instrum.*, 2020, **91**, 073111. https://doi.org/10.1063/5.0012669
21. J. Guezenoc, L. Bassel, A. Gallet-Budynek, and B. Bousquet, *Spectrochim. Acta B*, 2017, **134**, 6–10. https://doi.org/10.1016/j.sab.2017.05.009
22. S. Lu, S. Shen, J. Huang, M. Dong, J. Lu, and W. Li, *Spectrochim. Acta B*, 2019, **150**, 49–58. https://doi.org/10.1016/j.sab.2018.10.006
23. X. Huang, H. Xiao, X. Liu, Y. Liu, and H. Gao, *Microchem. J.*, 2025, **218**, 114805. https://doi.org/10.1016/j.microc.2025.114805
24. S. Wang, Y. Tang, P. Zou, E. Guo, Z. Yang, J. Liao, X. Zhang, T. Ni, and Z. Peng, *J. Anal. At. Spectrom.*, 2025, **40**, 3563–3568. https://doi.org/10.1039/d5ja00314h
25. Q. Yang, J. Mei, S. Feng, Y. Hang, W. Ma, C. Li, H. Qin, F. Shi, Z. Lu, C. Ye, and S. Yao, *J. Anal. At. Spectrom.*, 2026, **41**, 448–459. https://doi.org/10.1039/d5ja00372e
26. Q. Yang, J. Mei, W. Ma, S. Feng, Y. Hang, Z. Yu, F. Shi, H. Qin, C. Ye, Z. Lu, and S. Yao, *At. Spectrosc.*, 2024, **45**, 462–472. https://doi.org/10.46770/AS.2024.245
27. E. Van den Heuvel and Z. Zhan, *Am. Stat.*, 2022, **76**, 44–52. https://doi.org/10.1080/00031305.2021.2004922
28. M.P. Basilio, V. Pereira, and F. Yigit, *MethodsX*, 2024, **13**, 102890. https://doi.org/10.1016/j.mex.2024.102890
29. R. Rostamzadeh, M. Keshavarz Ghorabaee, K. Govindan, A. Esmaeili, and H.B.K. Nobar, *J. Cleaner Prod.*, 2018, **175**, 651–669. https://doi.org/10.1016/j.jclepro.2017.12.071
30. S. Opricovic and G.H. Tzeng, *Eur. J. Oper. Res.*, 2004, **156**, 445–455. https://doi.org/10.1016/s0377-2217(03)00020-1
31. M. Behzadian, S.K. Otaghsara, M. Yazdani, and J. Ignatius, *Expert Syst. Appl.*, 2012, **39**, 13051–13069. https://doi.org/10.1016/j.eswa.2012.05.056
32. H. Zhou, X. Wang, and R. Zhu, *Appl. Intell.*, 2022, **52**, 5457–5474. https://doi.org/10.1007/s10489-021-02524-x
33. J. Cheng, J. Sun, K. Yao, M. Xu, and Y. Cao, *Spectrochim. Acta A*, 2022, **268**, 120652. https://doi.org/10.1016/j.saa.2021.120652
34. C.M. Andersen and R. Bro, *J. Chemom.*, 2010, **24**, 728–737. https://doi.org/10.1002/cem.1360
35. N.L. Afanador, T.N. Tran, and L.M.C. Buydens, *Anal. Chim. Acta*, 2013, **768**, 49–56. https://doi.org/10.1016/j.aca.2013.01.004
36. J. Cheng and D. Sun, *Food Eng. Rev.*, 2017, **9**, 36–49. https://doi.org/10.1007/s12393-016-9147-1
37. S. Wold, M. Sjöström, and L. Eriksson, *Chemom. Intell. Lab. Syst.*, 2001, **58**, 109–130. https://doi.org/10.1016/S0169-7439(01)00155-1
38. H. Qin, Z. Yu, Z. Lu, Z. Yu, and S. Yao, *Appl. Spectrosc.*, 2022, **76**, 1123–1131. https://doi.org/10.1177/00037028221108416
39. GB/T 11170-2008, Stainless steel — Determination of multi-element contents — Spark discharge atomic emission spectrometric method (Routine method), 2008. https://openstd.samr.gov.cn/bzgk/gb/newGbInfo?hcno=F3D23071899B04720A72343807218D97&refer=outter